A New Two-Moment Bulk Stratiform Cloud Microphysics Scheme in the Community Atmosphere Model, Version 3 (CAM3). Part II: Single-Column and Global Results

A. GETTELMAN AND H. MORRISON

National Center for Atmospheric Research, Boulder, Colorado*

S. J. GHAN

Pacific Northwest National Laboratory, Richland, Washington

(Manuscript received 26 June 2007, in final form 4 January 2008)

ABSTRACT

The global performance of a new two-moment cloud microphysics scheme for a general circulation model (GCM) is presented and evaluated relative to observations. The scheme produces reasonable representations of cloud particle size and number concentration when compared to observations, and it represents expected and observed spatial variations in cloud microphysical quantities. The scheme has smaller particles and higher number concentrations over land than the standard bulk microphysics in the GCM and is able to balance the top-of-atmosphere radiation budget with 60% the liquid water of the standard scheme, in better agreement with retrieved values. The new scheme diagnostically treats both the mixing ratio and number concentration of rain and snow, and it is therefore able to differentiate the two key regimes, consisting of drizzle in shallow, warm clouds and larger rain drops in deeper cloud systems. The modeled rain and snow size distributions are consistent with observations.

1. Introduction

Clouds play a critical role in the climate system through their impact on the latent heating of the atmosphere and the radiative heating of the atmosphere and surface, as well as the hydrological cycle. Thus, clouds are critical in maintaining the global energy balance. For example, the response of subtropical oceanic stratocumulus clouds to climate change strongly affects shortwave cloud forcing globally, and different models produce responses of a different sign as sea surface temperatures change (Bony et al. 2006). The effects of aerosols on cloud particles may also have a significant impact on climate by modifying the cloud radiative properties, that is, indirect aerosol effects (Twomey 1977; Charlson et al. 1987), which have been analyzed recently by Lohmann et al. (2007), among many others. Given the importance of these interactions and the difficulty in parameterizing clouds due to the wide range of associated spatial and temporal scales, their treatment in large-scale models has been cited as the critical uncertainty in simulations of global climate and anthropogenic climate change (Stephens 2005).

Most current large-scale cloud schemes for global models do not have sufficient detail to represent these important interactions. Bulk schemes such as Rasch and Kristjansson (1998) or Rotstayn (1997) include prognostic variables for cloud liquid and ice mass, specification of the effective cloud particle size for treating radiative interactions, and limited treatment of mixed-phase processes. There are several motivations for developing a more advanced treatment of cloud microphysics that includes the prediction of both cloud particle number concentration and mass (i.e., a two-moment scheme) in a general circulation model (GCM). In addition to improving the representation of the microphysics, the treatment of both mass and number enables the mean cloud particle size to evolve in a more realistic manner, which is critical for radiative transfer as well as chemistry–cloud–aerosol interactions

* The National Center for Atmospheric Research is sponsored by the National Science Foundation.

Corresponding author address: A. Gettelman, National Center for Atmospheric Research, 1850 Table Mesa Drive, Boulder, CO 80305.
E-mail: andrew@ucar.edu

DOI: 10.1175/2008JCLI2116.1

such as wet deposition and scavenging. Two-moment schemes have been used for many years in mesoscale models and have only recently been implemented into GCMs (see discussion in Morrison and Gettelman 2008).

In this work we evaluate a new stratiform physics parameterization implemented in the National Center for Atmospheric Research (NCAR) Community Atmosphere Model (CAM). The scheme, described in detail in Morrison and Gettelman (2008, hereafter MG08), is a bulk two-moment scheme that predicts the mixing ratios and number concentrations of cloud droplets (liquid) and crystals (ice). This scheme includes a consistent treatment of microphysical processes, is appropriate for the coarse grid spacing of large-scale models, and is computationally efficient.

The key features of this scheme are detailed in MG08 and briefly summarized here. The scheme includes prognostic equations for number and mixing ratio of liquid and ice. It includes detailed and updated microphysical processes as described by MG08. It also includes an explicit representation of the mixed phase of vapor and ice by representing the Bergeron–Findeisen process of vapor deposition onto ice, liquid transfer to ice, and contact freezing. The scheme has a diagnostic representation of precipitation particle number concentration as well as mixing ratio. The scheme also includes activation of cloud droplets on aerosol coupled to a treatment of the subgrid vertical velocity. A detailed description of the formulations and numerical aspects of the scheme are given in Part I (MG08). In this paper, we describe the implementation of the scheme in CAM (section 2). We show evaluation of the scheme in a single-column version of the model in section 3, show global results in section 4, and describe the sensitivity of the scheme to key model elements in section 5. Conclusions are in section 6.

2. Model description

The scheme described by MG08 is implemented in the framework of CAM, version 3 (CAM3). CAM3 is described by Collins et al. (2006), and a complete technical description is contained in Collins et al. (2004). The base model uses a microphysical parameterization described by Rasch and Kristjansson (1998, hereafter RK98). RK98 is a bulk microphysical scheme with prognostic and conserved mass of ice and liquid. This scheme is closed with large-scale condensation assumptions described by Zhang et al. (2003). These assumptions provide the microphysics with the amount of condensed phase liquid and ice, and the microphysics converts this to precipitation. In the RK98 scheme, the fraction of new condensate that is ice is a fixed linear function of temperature, ramping from pure liquid at temperatures above $-10°C$ ($T > -10°C$) to pure ice for $T < -30°C$. The partitioning of ice condensate can vary slightly from this fixed function with differential sedimentation for liquid and ice in the RK98 scheme. CAM3 assumes that clouds can occupy a fraction of a grid box, and the fractional cloud scheme uses the diagnostic formulation of Slingo (1987).

To implement the MG08 scheme in CAM3, we have made several modifications to the model physics described above. We have replaced the microphysics of RK98 with that of MG08. In addition, we have adopted the Vavrus and Waliser (2008) changes to the Slingo (1987) scheme. The change is an empirical fit to observations of Arctic clouds and is described in more detail by Vavrus and Waliser (2008). Briefly, the change adjusts the cloud fraction (F) when the water vapor mixing ratio (q) is low, such that cloud fraction $F = (q/3.0) \times F$ when $0.45 < q < 3.0$ (q in g kg^{-1}), and if $q < 0.45$ g kg^{-1}, then the maximum permitted cloud fraction (F) is 0.15. It is designed to reduce model biases of almost total ($F = 1$) low Arctic cloud cover in winter in a low q environment. It is essentially an adjustment to the already ad hoc Slingo (1987) parameterization to reduce Arctic cloud biases. As a result, both model configurations with the RK98 and MG08 microphysics schemes are radiatively balanced.

In addition, the new microphysics scheme uses the mass and number of aerosols as input for calculating droplet nucleation. In the simulations presented here, we prescribe the aerosol distribution to isolate the impact and effect of the new microphysics. Monthly mean distributions of sulfate, soil dust, carbonaceous species, and sea salt are derived from a three-dimensional aerosol assimilation (Collins et al. 2001). The direct effect of aerosols on radiation follows Collins et al. (2002). The only additional modification we have made to the aerosols is to distribute the sea salt aerosol into a large (coarse) and small (accumulation) mode. Here, 86% (6/7) of the mass is in the coarse mode (Mahowald et al. 2006).

Droplet nucleation is related to the number, size, and composition of all aerosol types using the nucleation scheme of Abdul-Razzak et al. (1998) and Abdul-Razzak and Ghan (2000). Aerosol number is diagnosed from mass concentration for each aerosol type. For sulfate, the empirical relationship $N_a = 340(\mathrm{mSO_4})^{0.58}$ is used (Lohmann et al. 2000), where N_a is the number (cm^{-3}) and $\mathrm{mSO_4}$ is the mass of sulfate (μg m^{-3}). For other aerosol species, we use prescribed lognormal size distributions to diagnose number from mass. For organic and black carbon, the number mode radius is 0.02

and 0.01 μm, respectively, with $\sigma = 2.24$ and 2.0, respectively. For dust, the number to mass ratios is taken from sections of a lognormal with volume mode radius of 2.5 μm and $\sigma = 2$ applied to each of the four dust size bins, as described by Zender et al. (2003; values in their Table 2). For sea salt, the radius in the two bins is prescribed at 0.5 and 10μm (Mahowald et al. 2006). The resulting ratios are given in Table 1. The hygroscopicity of sulfate, sea salt, soil dust, and hydrophilic organic carbon is 0.51, 1.16, 0.14, and 0.14, respectively (Ghan et al. 2001); the hygroscopicity of black carbon and hydrophobic organic carbon is essentially zero.

We recognize that the assumed external mixing state of the aerosol (each aerosol type is distinct from the others) is unrealistic except near primary sources. This can affect the droplet nucleation efficiency of the hydrophobic species and hence can change the droplet number. Treating internal mixing of aerosol components would introduce ambiguities about size distribution unless the size distribution is predicted, which would require a separate effort.

The number of active ice nuclei in the new scheme is specified as a function of temperature, following Cooper (1986); there currently is no direct coupling between the ice nucleation and prescribed aerosol.

In addition, the model now uses the predicted mixing ratio and number concentration of cloud particles to diagnose an effective radius for both liquid and ice. These effective radii are input to the calculation of cloud optical properties, which follows Slingo (1989) for liquid and Ebert and Curry (1992) for ice. The range of effective radii is truncated in the radiation code only to match the valid radiation parameterization ranges. MG08 assumes spherical ice particles. In the absence of a clear formulation of the crystal habit for small ($R <$ 100 μm) crystals, we use the assumption of spheres as adopted by Heymsfield and Banssemer (2007). The assumption presents a slight inconsistency with the Ebert and Curry (1992) parameterization, which assumes hexagonal plates, but differences for small crystals are not large. Larger crystals are considered precipitation (snow) and are not included in the radiation code.

For the analysis of the scheme, we present both single-column experiments (section 3), global evaluation (section 4), and sensitivity tests (section 5).

3. SCAM results

The new microphysics parameterization has been implemented in a single-column formulation [the Single-Column Community Atmosphere Model (SCAM)], where the dynamics and horizontal advective tendencies are specified from observations or model analyses. Sensitivity tests of key parameters in the new scheme have also been performed using SCAM; results are similar to the global sensitivity tests described in section 5 and are therefore not shown here. Results for two intensive observing periods (IOPs) from the Atmospheric Radiation Measurement Program (ARM) Oklahoma Southern Great Plains (SGP) site are described below. These IOPs include the period from 1 to 22 March 2000, which consisted of a series of fronts and synoptic systems (Xie et al. 2005), and the period from 18 July to 4 August 1995, which consisted mostly of periods of deep convection typical of a continental summertime regime (Ghan et al. 2000).

TABLE 1. Scaling factors for aerosol mass to number(num) (units of num kg^{-1}).

Name	Scaling
Sulfate	Lohmann et al. (2000)
Sea salt (accumulation)	1.349e + 15
Sea salt (coarse)	2.330e + 12
Dust 1 (small)	3.484e + 15
Dust 2	2.138e + 14
Dust 3	2.205e + 13
Dust 4 (large)	3.165e + 12
Hydrophilic organic C	7.456e + 17
Hydrophilic black C	9.837e + 18
Hydrophobic organic C	7.456e + 17
Hydrophobic black C	9.837e + 18

Figure 1 illustrates output from a simulation with the new MG08 microphysics from the single-column model for a simulation of the March 2000 IOP at the ARM SGP site. Model output is compared to retrievals of ice and liquid described in Mace et al. (2006). Retrievals are averaged over the 20-min model time step. The model is able to simulate the general observed cloud features and distributions of liquid and ice. The magnitudes for liquid and ice are quite comparable, especially the much lower in-cloud ice water content (IWC) relative to liquid water content (LWC), and the fairly small LWC (generally LWC < 0.1 g m^{-3}) at mid- and upper levels. The main difference is that the simulation has more cloud at low levels, which is also present in the base (RK98) model simulation. The other difference is that the peak LWC and IWC in the retrievals tend to be larger than in the simulations. This is likely due to the fact that retrievals represent local (point) values and would be expected to have more variability than grid-mean values from the model.

Table 2 shows IOP averages for total precipitation rate, liquid water path (LWP), and ice water path (IWP) for the cloud retrievals obtained from ground-based remote sensors (millimeter cloud radar and microwave radiometer) and thermodynamic soundings,

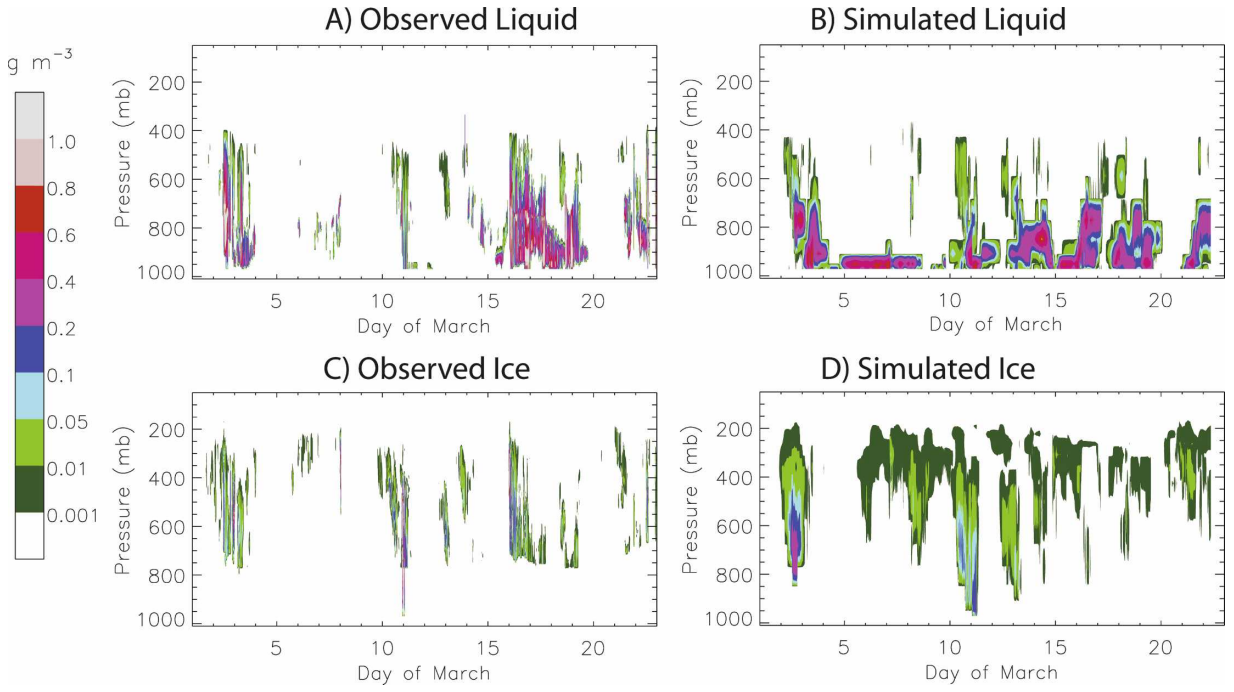

FIG. 1. (a),(c) Observed and (b),(d) simulated (a),(b) LWC and (c),(d) IWC for the March 2000 IOP at the ARM SGP site. Units of g m^{-3}.

the base case model run with RK98 microphysics and the model run with MG08 microphysics.The retrievals and error estimates are described by Mace et al. (2006) for IWP and Lesht and Liljegren (1997) for LWP. We note that there is considerable uncertainty in the LWP retrieved from microwave radiometers, especially due to collection of water on the radiometer during periods of precipitation (Mace et al. 2006). To avoid this problem we treat LWP as missing during periods when the surface precipitation exceeds 1 mm h^{-1}. Note that this likely results in a low bias of the LWP given that the LWP would be expected to be largest during the precipitation events.

The MG08 scheme has a higher LWP than retrieved in March 2000, but less than retrieved in July 1995. The quantities are in better agreement than with the RK98 scheme, which has very high LWP in both cases. The reduction of LWP using the MG08 scheme is consistent with the global results presented later. The LWP reduction results from different treatment of conversion of cloud water to precipitation (through autoconversion and Bergeron processes). There is slightly more snow [snow water path (SWP)] and less cloud ice in MG08 compared to RK98. This arises mostly because of differences in the autoconversion of ice crystals to snow (precipitation) in the MG08 scheme. Both MG08 and RK98 produce a total frozen water path (snow + cloud ice) in the simulations that is similar to the retrievals in Table 2 (which represent combined snow and ice). Total precipitation rates in MG08 are higher than in the RK98 scheme and larger than in observations. This may be related to the larger SWP. Note that there is lower IWP in the MG08 scheme in the July case (Table 2).

In addition to the basic statistics and the morphology shown in Table 2 and Fig. 1, the scheme is also able to capture unique features of specific regimes. In particular, it is able to differentiate between large rain drops formed primarily by melted snow in deep cloud systems versus drizzle in shallow warm clouds (Fig. 2). For example, from 10–11 March, a deep cloud with significant

TABLE 2. IOP period mean values from retrievals (Obs), base run with RK98 scheme and with new MG08 scheme. Shown in the table are total precipitation rate (mm day^{-1}), grid-mean LWP, grid-mean SWP, and grid-mean cloud IWP (all g m^{-2}) for IOP cases at the ARM SGP site. Note that the retrieved SWP includes ice particles of all sizes (i.e., both cloud ice and snow).

Simulation	Total precipitation	LWP	SWP	IWP
March 2000				
Obs	4.08	120	62.6	
RK98	4.87	275	32.2	21.4
MG08	5.05	231	42.8	9.3
July 1995				
Obs	7.58	112		
RK98	9.00	213	63.9	25.1
MG08	9.42	70.4	92.3	15.2

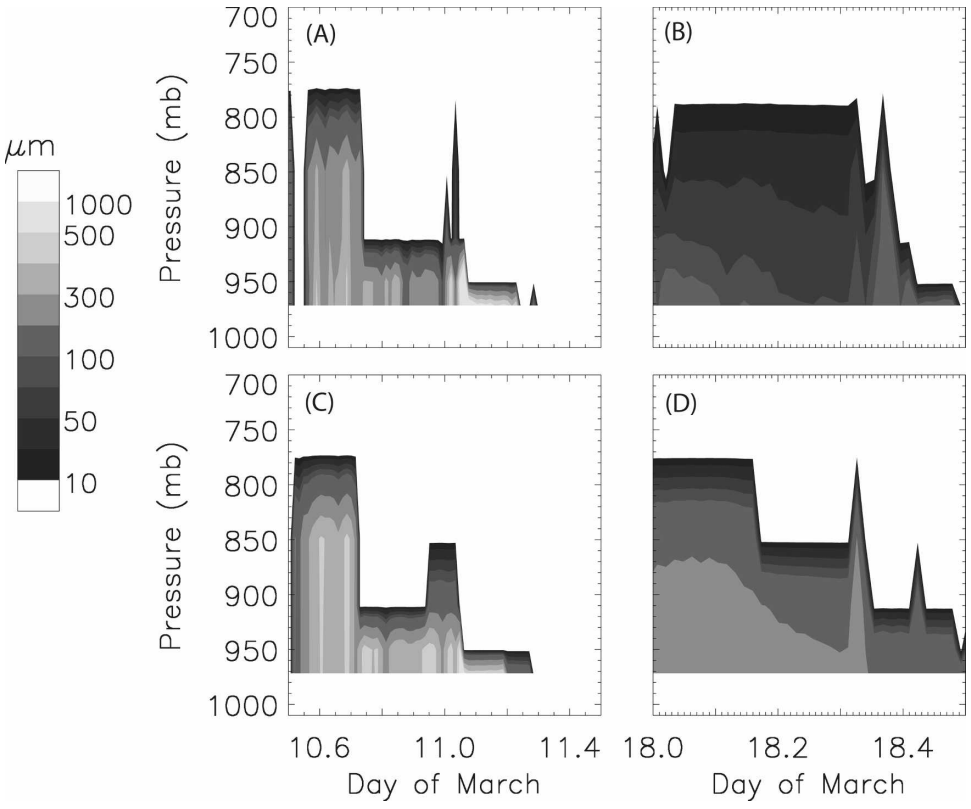

FIG. 2. Stratiform rain mean volume radius (μm) for (a), (c) 11 March and (b), (d) March 18 cases using the (a), (b) baseline MG08 scheme and (c), (d) sensitivity test with constant rain intercept parameter $N_0 = 10^7$ m^{-4} from SCAM simulations.

ice was observed (Figs. 1a,c). The MG08 simulation captures this event, which results in significant stratiform precipitation at the ground in the form of rain changing to snow, with a mean volume radius of rain greater than 200 μm and often exceeding 500 μm (Fig. 2a); the associated values of the rain size distribution parameters (e.g., intercept parameter and slope) are similar to those observed by Marshall and Palmer (1948) for midlatitude frontal systems. However, for the shallow, low-level warm clouds on 18 March (Fig. 2b), the model produces stratiform rain characteristics that are consistent with drizzle, with a mean volume radius of about 20 to 80 μm. These sizes are similar to in situ observations of drizzle reported by Wood (2005). Note that the model also produces extensive low-level warm clouds with drizzle between 5 and 8 March, which are not evident from the observations. These clouds also appear in the simulation with the RK98 microphysics; therefore, they do not occur as a result of differences between the MG08 and RK98 microphysics schemes. Rather, for these conditions, other forcings, from the large-scale dynamics or the boundary layer scheme, are more important than the microphysics.

The key point is that the MG08 scheme captures unique features of the cold, deep and warm, shallow, drizzling cases due to its inclusion of rain number concentration as well as mixing ratio. Most schemes do not keep track of the precipitation number concentration and instead assume a fixed precipitation particle size distribution intercept parameter, N_0. By including precipitation number concentration, the MG08 scheme has greater flexibility in the treatment of the rain size distribution, including an intercept parameter that varies in time and space. To test the impact of including the precipitation number concentration, we have run sensitivity tests using the MG08 scheme. The sensitivity tests do not calculate rain number concentration and instead assume a constant rain intercept parameter of 10^7 m^{-4} [similar to the value found by Marshall and Palmer (1948)]. An important point is that this sensitivity run produces cloud properties and radiative forcing similar to the baseline (not shown). This is evident for both the SCAM and global runs. However, there are significant differences in the mean volume radius and mixing ratio of rain between the sensitivity and baseline MG08 runs for the shallow drizzling cases, as shown in

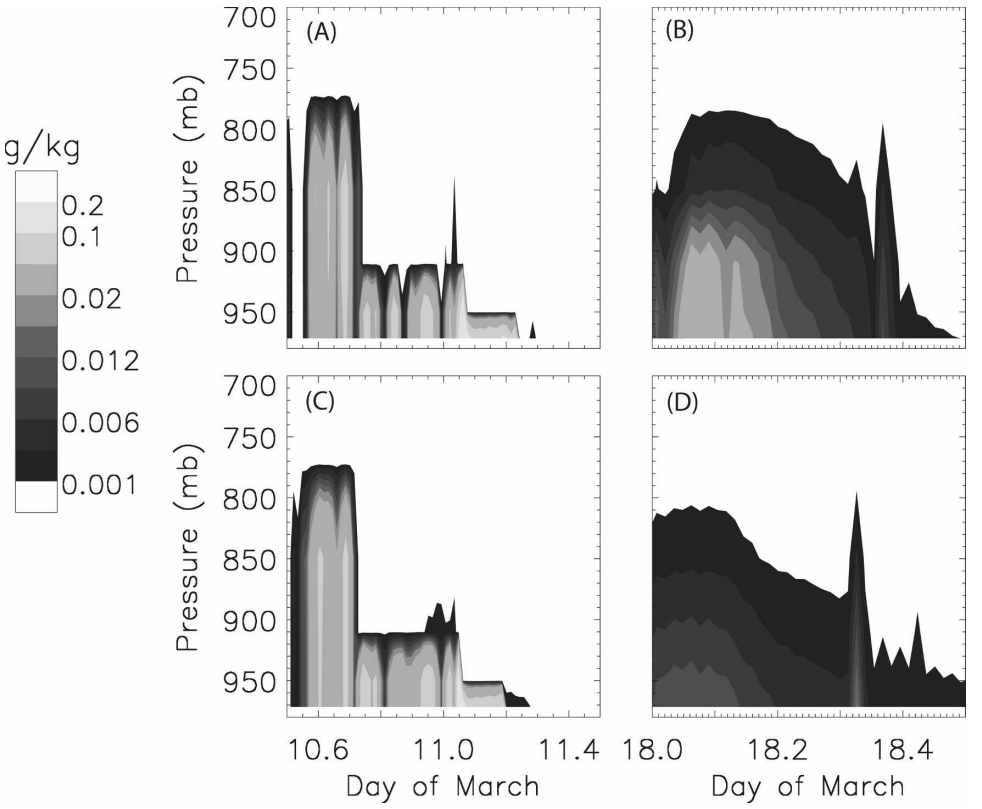

FIG. 3. Stratiform rain mean mixing ratio (g kg^{-1}) for (a), (c) 11 March and (b), (d) March 18 cases using the (a), (b) baseline MG08 scheme and (c), (d) sensitivity test with constant rain intercept parameter $N_0 = 10^7$ m^{-4} from SCAM simulations.

Figs. 2b,d, 3b,d. This occurs because the constant N_0 for rain of 10^7 in the sensitivity test is one to two orders of magnitude smaller than the variable N_0 for rain in the baseline run. Thus, the smaller N_0 in the sensitivity test leads to a volume mean radius of rain that is 2–5 times larger than it is in baseline; these larger sizes are inconsistent with observations of drizzle (e.g., Wood 2005). The larger rain size and hence mean fall speed in the sensitivity run subsequently leads to a reduced rain mixing ratio compared to baseline due to the more rapid sedimentation. Note that the sensitivity test is able to more closely reproduce baseline results for the cold, deep case (see Figs. 2a,c, 3a,c), because the variable N_0 in the baseline run is similar to the constant N_0 of 10^7 m^{-4} in the sensitivity test (not shown).

A similar sensitivity test, but using a fixed intercept parameter of 2×10^7 m^{-4} for snow instead of rain, produces results similar to baseline, both in terms of cloud properties and snow size distribution (not shown). Thus, inclusion of snow number concentration in MG08 appears to be less important than inclusion of rain number concentration. However, under conditions with small ice nucleus concentrations (observed in the Arctic by Prenni et al. 2007), the inclusion of snow number concentration may be important (Morrison and Pinto 2006). This is not an issue here because we assume fixed ice nucleus concentrations as a function of temperature (see MG08), but it could be important in the future if ice nucleus concentrations were predicted from the aerosol characteristics.

4. Global simulation results

Global simulations use prescribed aerosols as well as climatological sea and land surface temperatures for present-day conditions. The model is run using the finite volume (FV) dynamical core, a mass- and shape-preserving transport scheme based on Lin and Rood (1996). The hydrological cycle of this configuration with RK98 microphysics is described by Rasch et al. (2006) and Boville et al. (2006). Simulations are performed at $1.9° \times 2.5°$ horizontal resolution with 26 vertical levels and a model top at 2 hPa. The analysis averages 5 yr of model output after a 4-month spinup from initial conditions.

Figure 4 illustrates mixed-phase conditions using the

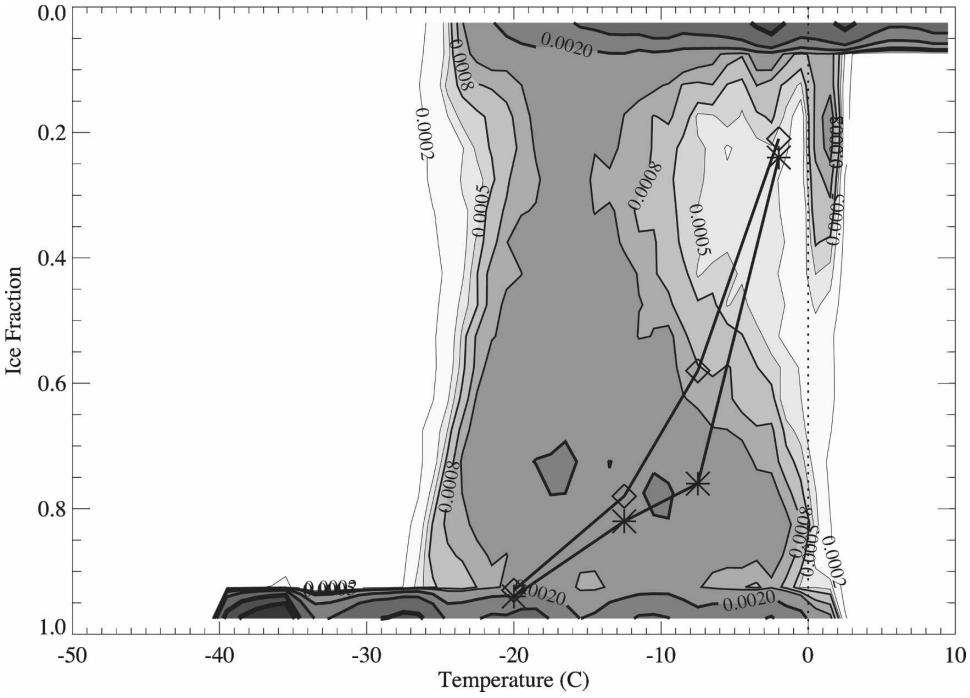

FIG. 4. Fraction of ice in version of CAM with new microphysics as a function of temperature. Symbols indicate observations by Field et al. (2005) for ice-dominated (diamonds) and liquid-dominated (asterisks) conditions.

MG08 microphysics scheme. In the MG08 scheme, the Bergeron–Findeisen process is represented by processes allowing for 1) vapor deposition onto ice and competition between ice and liquid condensation, 2) depletion of liquid onto ice, and 3) preferential evaporation over sublimation (see MG08, section 2b for details). Figure 4 is constructed for all points with greater than 2 ppm by mass (ppmm) of total in-cloud condensed water (liquid and ice), and both phases present (100% ice and 0% ice are excluded). Note that for the ice phase these plots include both cloud ice and snow, given that most of the ice mass in the model is from snow, and observations of ice mass generally include both large and small particles.

The transition between ice and liquid occurs most typically at about −17°C, but it can occur at a range of temperatures. Liquid can be present down to about −30°C, and ice exists for a few degrees above freezing (0°C) (in the scheme, snow melts at +2°C). Observations of liquid/ice fraction are rather limited, but the model agrees reasonably well with observations of Field et al. (2005), also noted in Fig. 4. The RK98 (base) version of CAM has a fixed linear ramp between liquid and ice from −10°C (all liquid) to −30°C (all ice), which is also in reasonable agreement with these results, but cannot capture the variability in ice fraction. Note that for ice fractions from 0.1–0.4, this is made up of two modes: one just above 0°C and one near −17°C, the mean of which is not far from the observations. The "warmer" mode is likely melting ice, while the "colder" mode is likely due to freezing processes. Thus the single average for the observations may hide variability of processes.

Figure 5 illustrates probability density functions (PDFs) for cloud particle effective radii and in-cloud number concentrations. In Fig. 5, similar to Fig. 4, a threshold of 2 ppmm is applied for in-cloud water or ice content, and the PDFs represent 950–100 hPa in the atmosphere. The PDFs are segmented between land and ocean points to highlight differences. For reference, diagnostic particle sizes from the base case for liquid and ice are shown in Figs. 5a,b (dotted). Note that in the RK98 version of CAM there are two sets of radii: one used for microphysical processes (such as sedimentation for ice) and one used by the radiation. We show the latter in Fig. 5. The base model (RK98) simulation specifies droplet sizes at 14 μm over the ocean and 8 μm over land, with a linear ramp between these for "mixed-phase" conditions over land between −30° and −10°C (Collins et al. 2004). Thus, when integrated in the vertical, over land particles in the RK98 scheme are mostly 14μm (frequency 0.4) and over ocean the frequency is 0.6. Crystal sizes are a function of temperature (RK98).

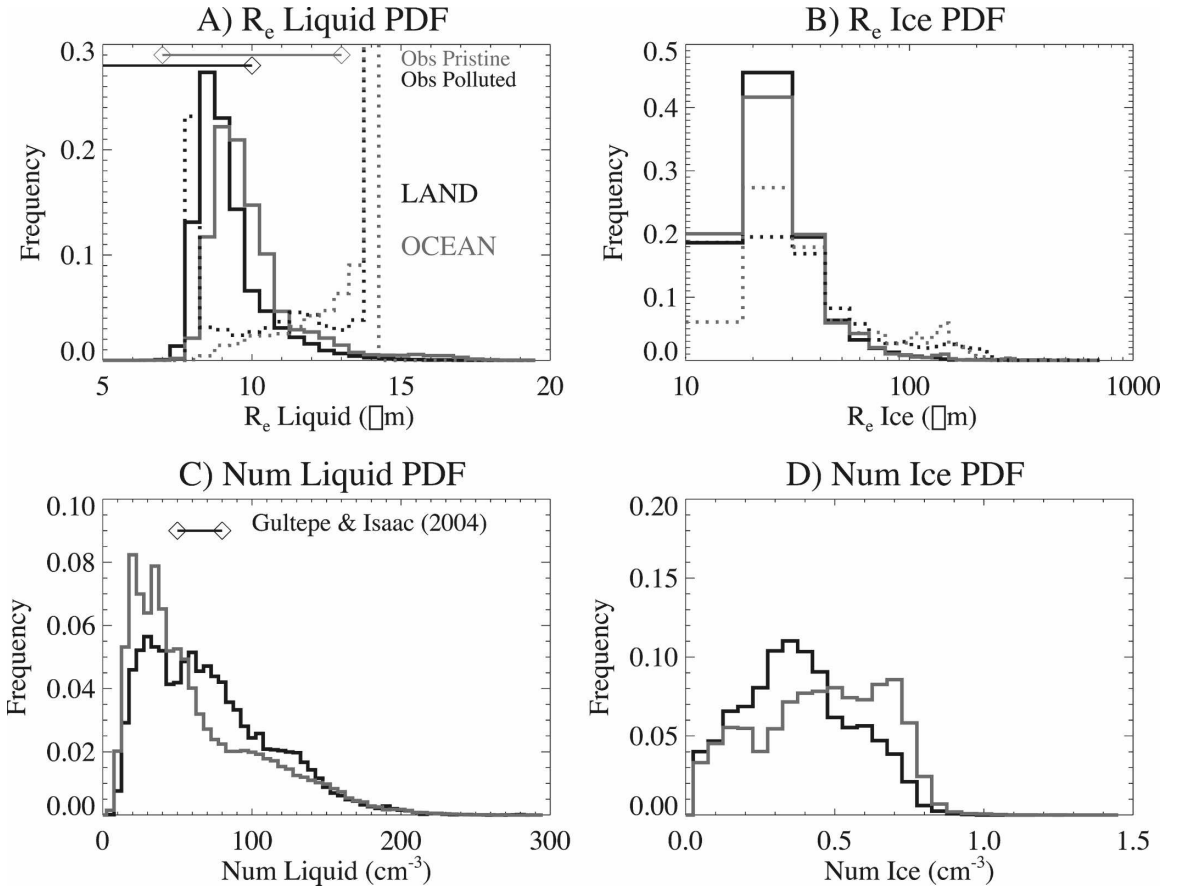

FIG. 5. PDFs of tropospheric (a) cloud droplet (liquid) effective radius, (b) cloud ice effective radius, (c) in-cloud droplet number concentration, (d) in-cloud ice number concentration. Land (black), ocean (gray), model with new microphysics (solid), and base code (dotted), with diagnostic size [(a) and (b) only]. Lines and diamonds in (a) denote range of observations of in situ liquid effective radius for polluted (black) and pristine (gray) conditions from previous studies noted in the text. Line and diamonds in (b) denote range of number concentrations from Gultepe and Isaac (2004).

The new MG08 scheme shows a clear distinction in droplet (liquid) sizes between land and ocean (Fig. 5a), with ocean points having significantly larger-mode particle size, and slightly lower number concentrations (Fig. 5c). The number concentration peaks at about 20–30 cm^{-3} over ocean, with a broad peak between 30 and 90 cm^{-3} over land. Values exceeding 100 cm^{-3} occur frequently over both land and ocean, while values greater than 200 cm^{-3} are much less common. These concentrations are smaller than specified in RK98 for some of the microphysical process rates. RK98 assume that the number concentration for liquid drops is 400 cm^{-3} over land, 150 cm^{-3} over ocean, 75 cm^{-3} over sea ice, and some ramping between these values for coastal regions. The mode size of liquid drops with the MG08 microphysics is about 8–10 microns, which is much smaller than the base model (RK98) size of 14 microns over the oceans. These values compare well with various in situ observations, with values between about 4–10 μm in polluted versus 7–13 μm in pristine conditions (Bower and Choularton 1992; Martin et al. 1994; Brenguier et al. 2003; Pawlowska et al. 2006), also shown in Fig. 5a. Most of these studies (except Bower and Choularton 1992) are from warm boundary layer stratocumulus, where much of the sampling has taken place. Ground-based remote retrievals of effective radius give a similar range of values (6–12 μm) for liquid boundary layer clouds over land and ocean (Kim et al. 2003; Sengupta et al. 2003). Reports in the literature of droplet effective radius in mixed-phase clouds are rather limited, but observations in the Arctic are similar to measurements for warm clouds, with values of about 3–7 μm in polluted (Zuidema et al. 2005) and 6–14 μm in pristine (McFarquhar et al. 2007) conditions. Cloud drop numbers (Fig. 5c) are peaked from 30–100 cm^{-3}, lower over ocean than land. This compares reasonably well with continental observations of 50–80 cm^{-3} from several aircraft campaigns reported by Gultepe and

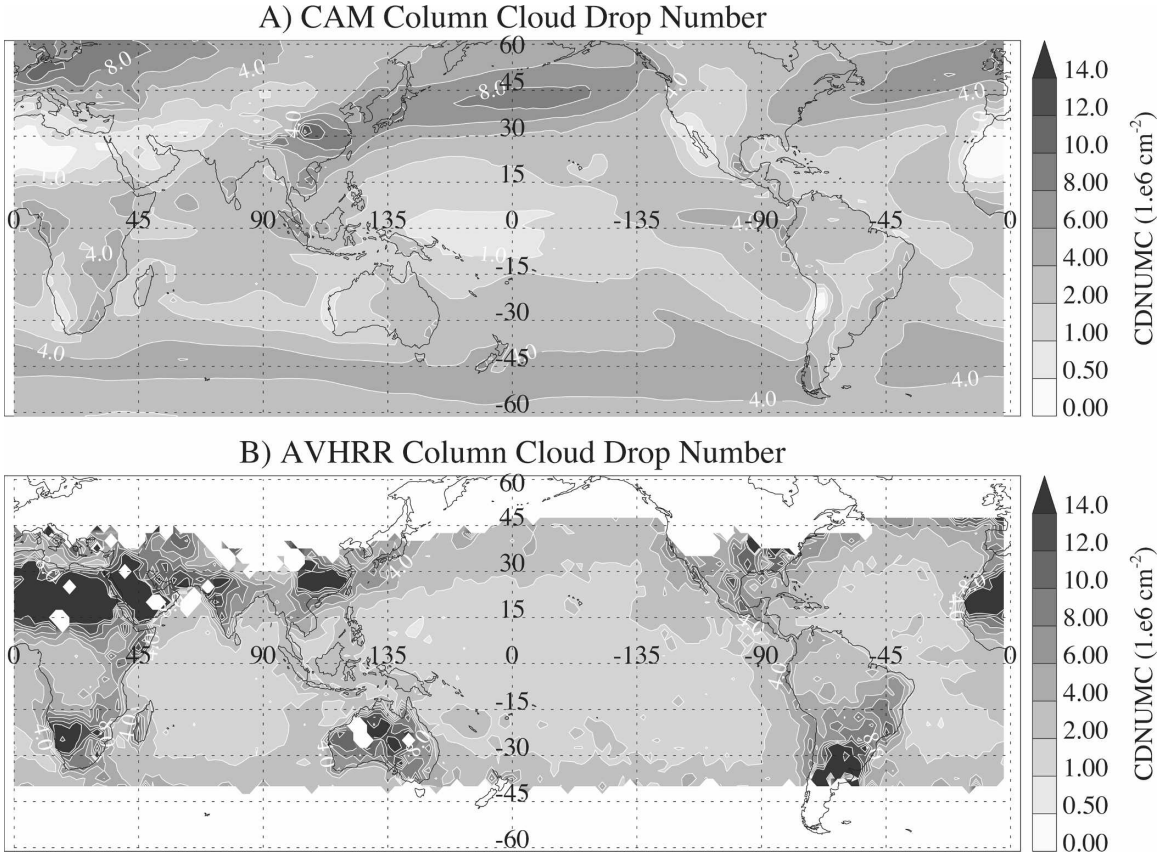

FIG. 6. Annual Mean 60°S to 60°N column cloud droplet number concentration in 10^6 cm^{-2} (10^{10} m^{-2}) from (a) CAM and (b) AVHRR.

Isaac (2004), also shown in Fig. 5c. We discuss comparisons with satellite retrievals against cloud top from the model below.

For ice (Figs. 5b,d), the peak effective radius is between 20 and 30 microns, similar to specified values in the RK98 scheme. Number concentrations are broadly distributed up to about 0.8 cm^{-3}, with higher concentrations over the oceans. This is due largely to the frequent presence of smaller crystals at high altitudes in the tropics, which is mostly ocean. Most of the particles larger than 40 microns are found outside of the tropics, where there is less detrainment of ice from deep convection. There is a long tail of large ice particles, with a few percent of crystals found at 100 microns or more. The upper limit of mean cloud ice particle sizes is limited by the conversion to snow. In situ observations of cloud ice are uncertain due to the difficulty of measuring small ice particles. Estimates of typical small ice particle concentrations reported in the literature vary by several orders of magnitude (Heymsfield 2007).

Figure 6 illustrates the column (vertically integrated) grid-mean cloud droplet number from the MG08 microphysics scheme (Fig. 6a) and Advanced Very High Resolution Radiometer (AVHRR; Fig 6b) retrievals (Han et al. 1998). Column cloud drop numbers are higher in storm track regions (with deepest cloud layers) and highest in the Northern Hemisphere downwind of aerosol sources over Europe, China, and North America. Cloud drop numbers are lower over tropical oceans and over dry subtropical regions. There are also very low column cloud drop numbers over ice sheets (Greenland and Antarctica) because of the limited amounts of liquid cloud in these regions. In general, the patterns and quantitative values agree well with column drop number retrievals from AVHRR data (Han et al. 1998), where available (within 40° latitude of the equator). The major difference is that AVHRR data (Fig. 6b) has anomalously high values over deserts, which Han et al. (1998) attribute to incorrectly retrieving dust particles as cloud droplets.

The vertical structure of particle size and in-cloud number concentration for liquid and ice is illustrated in Fig. 7. Low tropical clouds have smaller droplet size than at higher latitudes (Fig. 7a). Droplet number con-

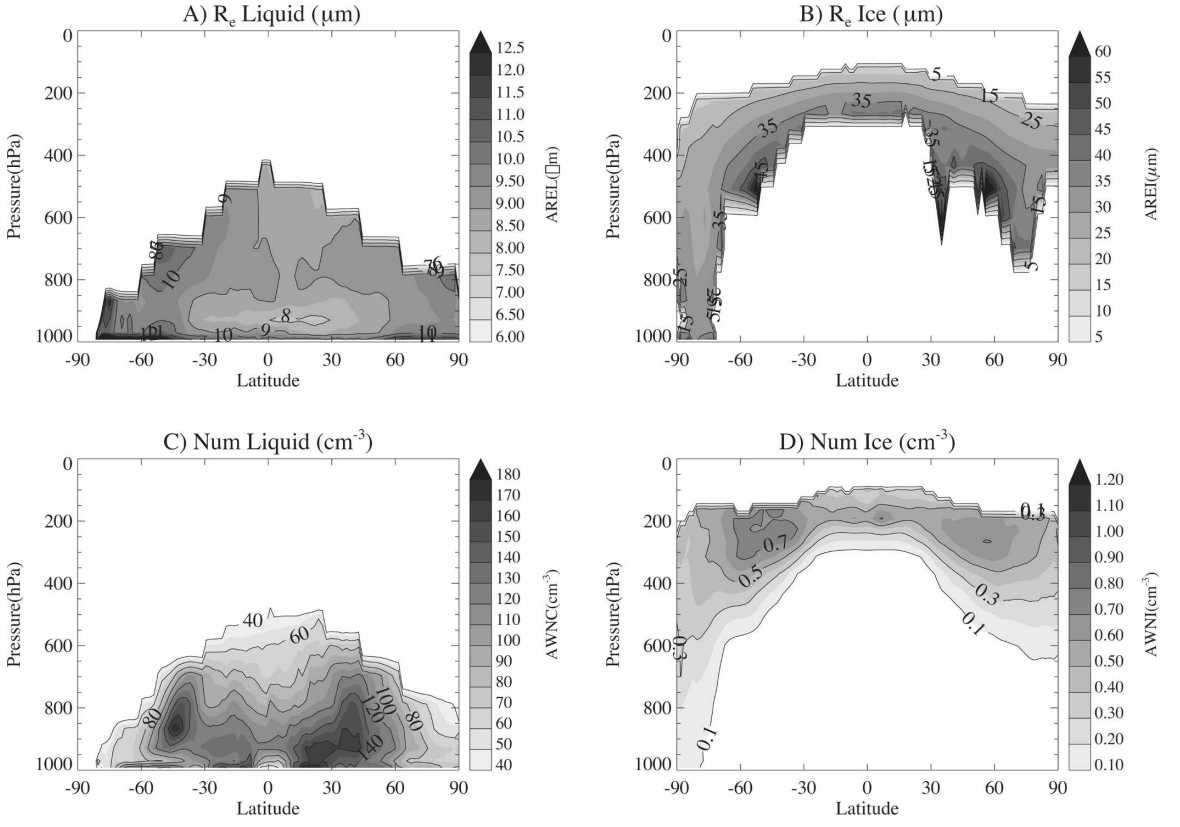

FIG. 7. Annual zonal-mean (a) cloud drop (liquid) effective radius (μm), (b) cloud ice effective radius (μm), (c) in-cloud droplet number concentration (cm^{-3}), (d) in-cloud ice number concentration (cm^{-3}) as a function of latitude and height.

centrations are highest in storm track regions (Fig. 7c), at about 850–900 hPa. The Southern Hemisphere pattern in Fig. 6 is more zonal, so the zonal mean in Fig. 7c has a slightly higher peak than in the Northern Hemisphere, though regional column values in the Northern Hemisphere are higher (Fig. 6). For ice, there is a broad distribution of crystal sizes, with a significant region of small ice crystals in the upper troposphere, and larger crystals in higher altitude regions of the midlatitude storm tracks (Fig. 7b). Ice crystal number (Fig. 7d) peaks in storm track regions at about 250 hPa.

The subgrid vertical velocity and cloud condensation nuclei (CCN) concentration, the two key components of droplet activation in the scheme, are shown in Fig. 8.

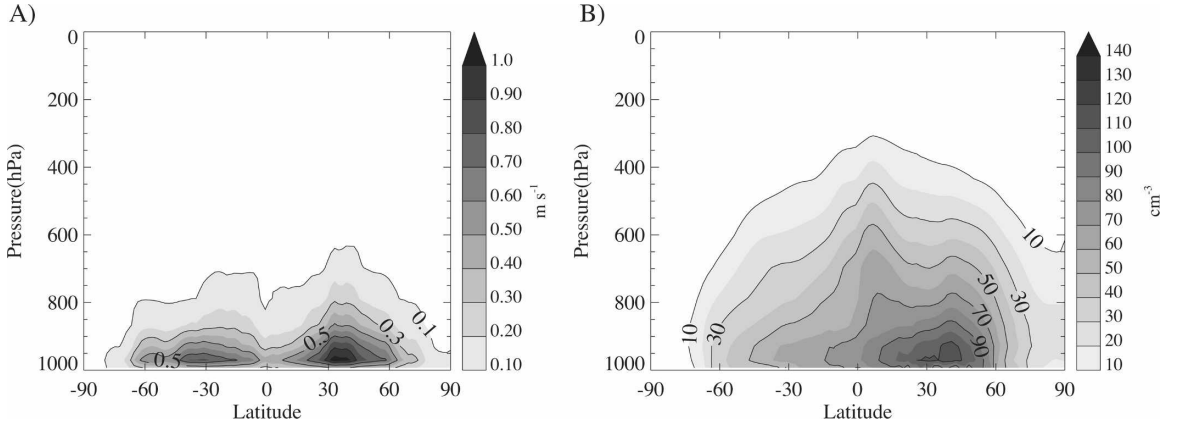

FIG. 8. Annual zonal-mean (a) subgrid vertical velocity (m s^{-1}) and (b) CCN concetnration (cm^{-3}) at (0.1%) supersaturation.

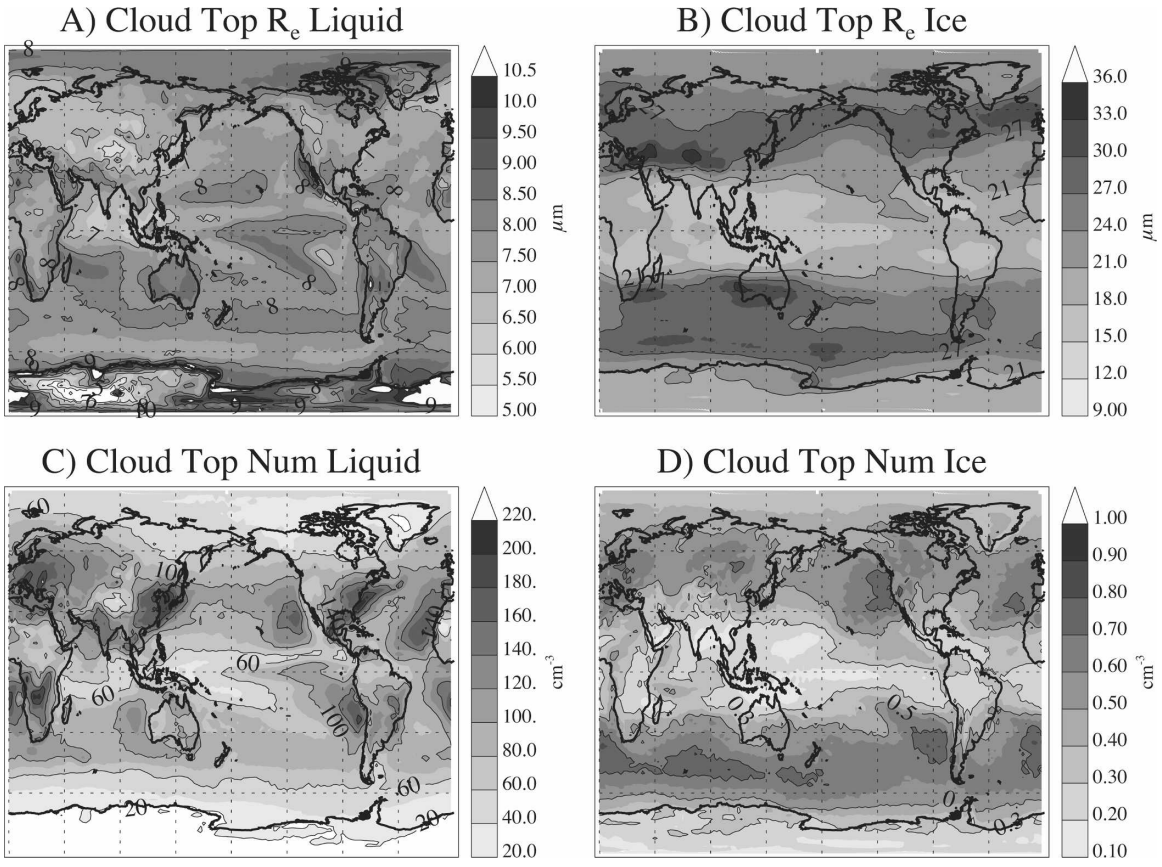

FIG. 9. Annual mean cloud-top (a) cloud drop (liquid) effective radius (μm), (b) cloud ice effective radius (μm), (c) in-cloud droplet number concentration (cm^{-3}), (d) in-cloud ice number concentration (cm^{-3}).

Figure 8 shows that the subgrid vertical velocity (diagnosed from the eddy diffusion coefficient) decreases with height. The largest values are in the storm track regions of each hemisphere, with values exceeding 1 m s^{-1} in the Northern Hemisphere.

Figure 8b illustrates the zonal mean cloud condensation nuclei concentration diagnosed at 0.1% supersaturation. The distribution is strongly peaked in the Northern Hemisphere midlatitudes because of the higher aerosol loading and higher subgrid vertical velocities. Higher CCN leads to relatively high droplet concentrations in these regions (Fig. 7c).

Figure 9 presents maps of in-cloud number concentration and effective radius diagnosed at cloud top. At each time step, values for the first cloud level counting down from the model top with more than 1 ppmm of condensate are output, for either ice or liquid, as appropriate. If ice is found, no liquid top is reported. In general, droplet sizes (Fig. 9a) are largest over ocean regions and smaller over the continents, as well as in regions of low-level stratocumulus clouds. There is slightly more distinction between regions if vertical averages over the depth of the cloud are examined, rather than cloud top. Droplet number concentrations (Fig. 9c), like column cloud drop number in Fig. 6, peak in regions with high aerosol loading in the Northern Hemisphere and in stratocumulus regions. High values in stratocumulus regions reflect the fact that these regions have a relatively low cloud-top height that is within the region of the lower troposphere with higher aerosol loading and hence greater CCN concentrations (Fig. 8b).

The spatial distribution of particle sizes and number concentrations agrees well with satellite observations, which are illustrated in Fig. 10. Moderate Resolution Imaging Spectroradiometer (MODIS) data is from retrievals of size and drop number by Wood et al. (2008). We note that in the absence of a full satellite simulator for the model, comparisons of satellite retrievals of cloud microphysical properties at cloud top to simulated cloud-top quantities are highly uncertain. There are several reasons for this. The major reasons are due to sampling of cloud top and sampling of particles. In the model, cloud top is the grid-box average of the

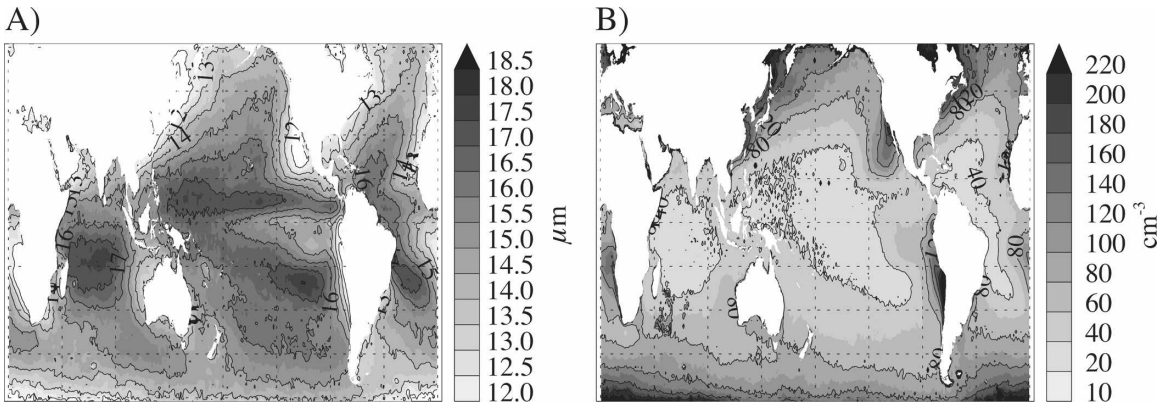

FIG. 10. Annual mean MODIS cloud-top (a) cloud drop (liquid) effective radius (μm) and (b) droplet number concentration (cm^{-3}). Data from retrievals processed by Wood et al. (2007).

highest liquid cloud layer (for liquid), representing 0.5–1.5-km thickness. Brenguier et al. (2003) clearly show that over 250-m vertical distance in a cloud, the particle size can vary from 6–12 μm. For optically thick clouds, the satellite will see larger particles than the model average for a larger layer. Second, the modeled values in Fig. 9 include only stratiform cloud particles, while the satellite retrievals make no distinction in cloud type or between cloud droplets and precipitation. Excluding precipitation will likely lead to smaller simulated effective radius, and including convective clouds (for which the model convective scheme does not provide a particle size) may also affect the results. Note that precipitation particles may also be sampled by in situ instruments (though they are likely excluded by the sampling method). The complexities of accounting for precipitation particles have been discussed by Wood (2000). For these reasons we use the satellite measurements to examine spatial distributions and gradients of particle numbers and sizes. Quantitative comparisons are highly uncertain in the absence of a detailed satellite retrieval simulator.

Satellite observations from MODIS indicate similar distributions of the droplet effective radius (Fig. 10a). Note the different scales between Fig. 9a and Fig. 10a. Largest sizes are over the oceans, especially in the subtropics. MODIS distributions of number concentration inferred from size and LWP (Fig. 10b) are also similar to Fig. 9c. However, the modeled cloud-top droplet effective radii are generally smaller than satellite retrievals, by 20% (versus AVHRR, not shown) to 50% (versus MODIS; Fig. 10a). This is likely due to the reasons noted above. The modeled values of droplet effective radius throughout the depth of a cloud are more consistent with in situ observations reported in the literature (Fig. 5a), as described previously. Cloud ice effective radius at cloud top (Fig. 9b) is largest in midlatitudes, because tropical cloud tops are at high altitude with generally small particles. Ice number concentration (Fig. 9d) also peaks in midlatitudes, with larger numbers of crystals in the Southern Hemisphere. It is not obvious why this occurs, but it could be due to more liquid water available for freezing in the Southern Hemisphere.

One of the unique features of this scheme is the diagnosis of rain and snow number concentrations in addition to the mixing ratios. Figure 11 illustrates the in-precipitation mixing ratio and number concentration for rain (liquid precipitation) and snow (solid precipitation). Not surprisingly, maxima are found in storm track regions. The highest number concentrations in storm track regions for rain (Fig. 11c) exceed 1001^{-1} in the Southern Hemisphere between 700 and 800 hPa, and 701^{-1} in the Northern Hemisphere at similar altitudes. These rain mixing ratios and number concentrations produce a zonal-average drop mean volume radius of about 70–200 μm, which is between the values observed for drizzle (see Table 4 in Wood 2005) and values for rain drops in deeper cloud systems described by a Marshall–Palmer distribution (Marshall and Palmer 1948). As illustrated in Fig. 2, the model is able to differentiate between these two regimes when individual cases, rather than zonal and temporal averages, are examined. Snow numbers are high near the tropical tropopause, where small crystals are detrained from convection, and reach 51^{-1} in the mid- and upper troposphere. These snow number concentrations and mixing ratios give values of the slope parameter of the snow size distribution (equal to the inverse of the mean number-weighted snow particle size) of about 10–100 cm^{-1}; these values are broadly consistent with in situ observations (e.g., Fig. 5 in Houze et al. 1979; Fig. 5 in Heymsfield 2003).

The more complete description of clouds presented

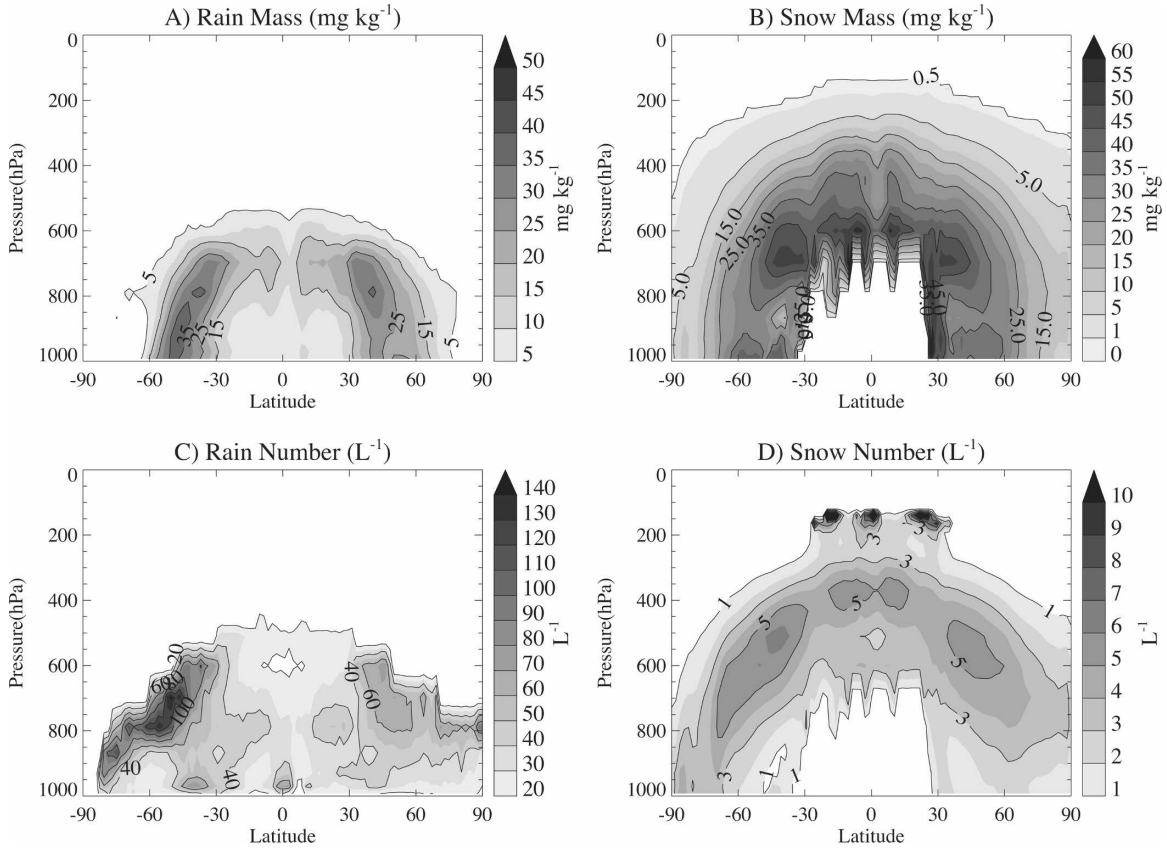

FIG. 11. Annual zonal-mean latitude height plots of (a) in-precipitation rain mixing ratio (mg kg^{-1}), (b) in-precipitation snow mixing ratio (mg kg^{-1}), (c) in-precipitation rain number concentration (1^{-1}) and (d) in-precipitation snow number concentration (1^{-1}).

above has obvious implications for the simulation of clouds globally and for global climate. Figure 12 illustrates zonal mean results from the simulation with the microphysics scheme of MG08, compared to the base model with microphysics from RK98, as well as available observations. Globally averaged summaries of these variables and others are contained in Table 3.

In general, global simulations with the MG08 scheme compare well to the RK98 scheme and to observations. This is not surprising, given that the model codes are the same in all respects except for the 1) stratiform microphysics, 2) drying of clouds at low specific humidities [the changes described by Vavrus and Waliser (2008) discussed in section 2], and 3) different relative humidity (RH) thresholds for fractional cloudiness to achieve levels of total cloud that balance the top-of-atmosphere (TOA) radiation (the minimum RH for cloud formation is 0.92 for MG08 and 0.90 for RK98). Both the MG08 and RK98 schemes use the same macrophysical closure of fractional condensation from Zhang et al. (2003). Thus, differences between the schemes result from differences in the parameterization of conversion between liquid and ice as well as the precipitation processes, and from slight changes to the cloud fraction, but not from differences in the parameterization of condensate production/evaporation.

Figures 12a,b illustrate the shortwave cloud forcing (SWCF; Fig. 12a) and the longwave cloud forcing (LWCF; Fig. 12b). Values compare well to observations from the Clouds and the Earth's Radiant Energy System (CERES) retrievals, except for higher magnitude shortwave forcing in the subtropics and longwave forcing in the tropics, which is also a feature of the RK98 scheme. The anomalous forcing is likely related to biases in cloud distributions in the tropics and subtropics. These biases are not governed by the stratiform microphysics. The MG08 scheme has a total (shortwave plus longwave) cloud forcing that is nearly the same as in RK98, but the magnitudes of both the shortwave and longwave forcings are reduced by about 1 W m^{-2}, in better agreement with observations (Table 3).

The zonal-mean, grid-mean column (vertically integrated) cloud droplet number concentration (Fig. 12c) peaks in the storm track regions and is higher in the Northern Hemisphere, consistent with Fig. 6. Compared to retrievals of column number from Han et al.

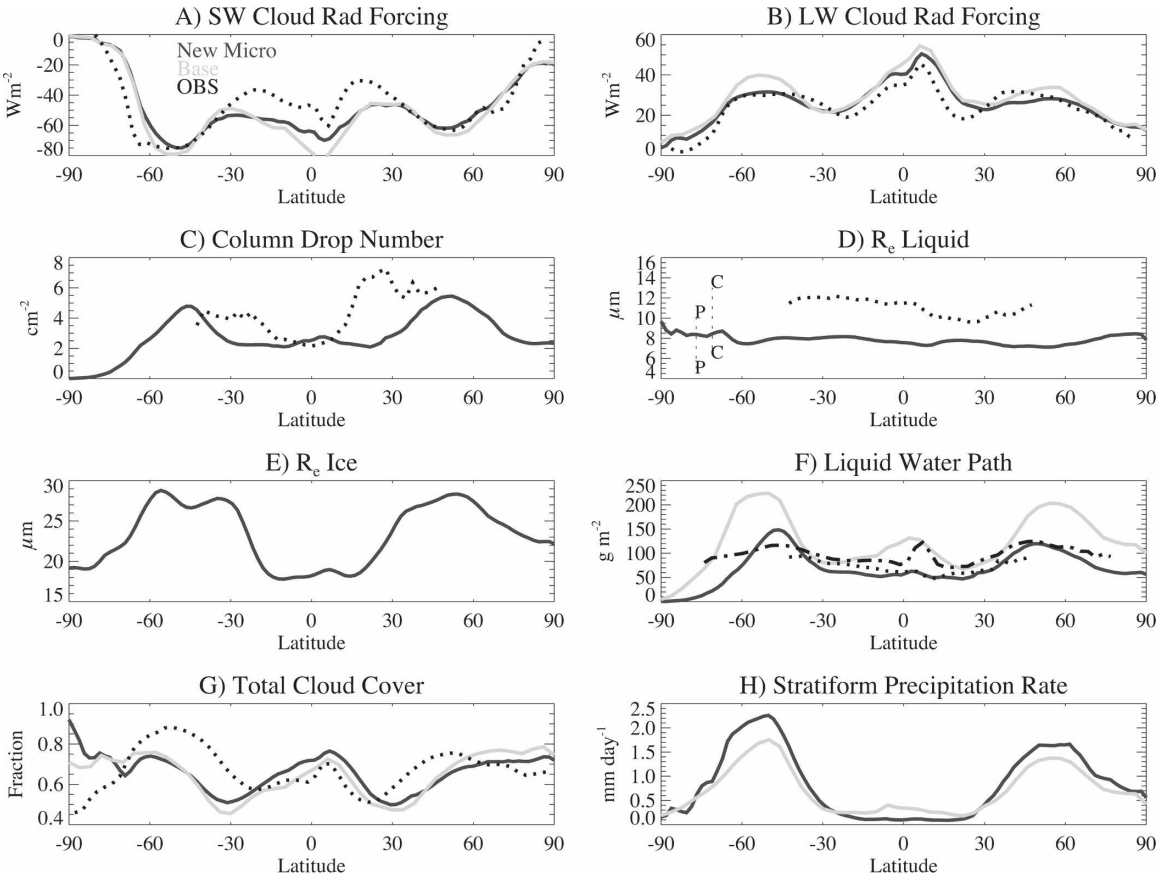

FIG. 12. Zonal-mean values from base (light gray), new microphysics (dark gray), and observations (black dotted). Variables shown are (observations noted in parentheses and in text): (a) shortwave cloud forcing (CERES), (b) longwave cloud forcing (CERES), (c) column cloud drop number concentration (AVHRR) (d) cloud-top effective radius liquid [AVHRR: thick line; in situ observation ranges for polluted (P) and clean (C) shown with thin line at arbitrary latitude), (e) cloud-top effective radius ice, (f) LWP (AVHRR: dotted; SSMI: dotted–dashed), (g) total cloudiness (ISCCP), and (h) stratiform precipitation rate.

(1998), the model reproduces the tropical value and the extratropical peaks (including the hemispheric differences), but with peaks that are at higher latitude (observations are only available for latitudes equatorward of about 45°). The reason for this discrepancy is likely because the AVHRR data include dust as cloud droplets; thus, over subtropical deserts (most prominently the Sahara Desert), very high anomalous number concentrations are recorded (Han et al. 1998).

The zonal-mean distribution of cloud-top effective radius for liquid clouds (Fig. 12d) varies only slightly with latitude, which hides the regional variations seen in Fig. 9a. The global-mean value for liquid clouds is 7.7 μm (Table 3). This value is about 25% smaller than the average cloud-top effective radius from AVHRR data (10.5 μm). As noted previously, direct comparison of the modeled and satellite values of cloud-top effective radius is complicated by differences in vertical scale between the model (uniform over the model level of $\sim$1 km) and satellite retrievals ($\ll$1 km), as well as convective cloud and precipitation particles. The values are in agreement with in situ and ground-based cloud radar observations. The range of in situ observations from Fig. 5a has been replotted on the side for clean and polluted conditions in Fig. 12d (designated C and P, respectively).

The most striking difference between results using the base RK98 model and the MG08 microphysics scheme is a significant reduction in the grid-mean cloud liquid water path (Fig. 12f), especially over midlatitude storm track regions. The model with the MG08 scheme is able to achieve similar radiative forcing as with RK98, using much smaller water paths because the average cloud droplet effective radius tends to be much smaller than assumed by the RK98 scheme (Figs. 5a,b). This reduced liquid water path is in better agreement with many observations, for example, from AVHRR and Special Sensor Microwave Imager (SSM/I) data

TABLE 3. Annual global-mean values from various runs. Shown in the table are grid-mean IWP, grid-mean LWP compared to MODIS and AVHRR data, grid-mean cloud drop number concentration (CDNUMC) compared to AVHRR data, cloud-top effective radii for liquid and ice (CTRe) compared to AVHRR observations (liquid only), total precipitation rate ($\mathbf{P}_{tot}$) compared to the Global Precipitation Climatology Project (GPCP) and stratiform precipitation rate only ($\mathbf{P}_{strat}$). Also shown are SWCF and LWCF compared to CERES and Earth Radiation Budget Experiment (ERBE) observations, and net TOA (NetTOA) radiation budget.

Simulation	RK98	MG08	Step1	Step3	Wsub40	No-QVar	NumCol	OBS
IWP (g m^{-2})	15	7.1	5.8	6.4	7.0	7.1	7.0	
LWP (g m^{-2})	123	73.5	74.1	75.5	73.5	88.3	69	64–155
CDNUMC (10^6 cm^{-2})		2.98	3.18	3.02	2.98	3.28	2.92	4
CTRe$_l$ (μm)		7.7	8.3	7.8	7.8	9.1	7.7	10.5
CTRe$_i$ (μm)		23.1	22.0	23.1	22.8	22.9	22.9	
Cld$_{tot}$ (%)	59	64	63	63	63	63	64	67
$\mathbf{P}_{strat}$ (mm d^{-1})	0.94	0.73	0.70	0.74	0.73	0.73	0.71	
$\mathbf{P}_{tot}$ (mm d^{-1})	2.90	2.90	2.92	2.92	2.91	2.91	2.90	2.61
SWCF (W m^{-2})	−55.9	−54.9	−53.1	−55.1	−54.9	−54.5	−55.2	−54 to −49
LWCF (W m^{-2})	30.7	29.5	27.6	29.2	29.4	29.5	29.4	27–30
NetTOA (W m^{-2})	−0.26	−0.04	1.1	−0.44	−0.07	−0.46	−0.49	

(the latter over ocean) shown in Fig. 12f. Also, the storm track peaks in liquid water path are shifted equatorward relative to the RK98 case. AVHRR- and SSMI-retrieved liquid water paths are significantly less than those from MODIS (the high end of the range for LWP in Table 3).

There are slight changes in total cloudiness using the MG08 scheme as seen in Fig. 12g. Some of these changes result from tuning of the macrophysical (cloud fraction) formulation to bring the TOA radiation into balance; in the code, the total cloudiness is adjusted by modifying the threshold for cloud formation in the fractional cloudiness scheme of Slingo (1987). In this case, the thinner (i.e., less liquid water path) clouds using the MG08 microphysics scheme actually have a higher relative humidity threshold for formation, but they are slightly more frequent over all regions except the Arctic. The increase in cloud cover globally is in slightly better agreement with observations from the International Satellite Cloud Climatology Project (ISCCP; Table 3), but the tropics is slightly worse. This change is likely due to different treatment of cirrus cloud and anvil microphysics in the MG08 scheme.

The average grid-mean precipitation rate (Table 3) is nearly identical in the two simulations; however, the stratiform precipitation rate produced by the MG08 microphysics (Fig. 12h) is nearly 20% lower, particularly in the tropics and subtropics, where there is much less stratiform precipitation. This reduced stratiform precipitation rate is compensated for by an increase in the convective precipitation rate. Note that the stratiform precipitation rate in the tropics and subtropics is much smaller than the convective precipitation rate in both simulations.

We have also examined simulations with elevated sea surface temperatures to try to understand if the model climate sensitivity is altered by the change in liquid water. It has been shown that a strong determinant of climate sensitivity in a GCM is the response of the system to the change in low clouds (Bony et al. 2006). This shortwave cloud feedback (the change in SWCF) is negative in CAM. That is, as the planet warms due to enhanced CO_2, the shortwave cloud forcing (which is negative, a cooling) increases.

To assess changes to the cloud feedbacks, we perform a sea surface temperature (SST) perturbation experiment similar to that described by Cess et al. (1990). SSTs are incremented globally by +2°K. Ringer et al. (2006) show that an SST perturbation experiment generally produces a similar response in the same model to a full climate sensitivity experiment. To perform the experiment, two additional simulations were run with +2°K and 1) RK98 microphysics and 2) MG08 microphysics. We evaluate the changes between the 0° and +2°K experiments with each scheme. When SSTs increase, the TOA radiation flux drops because of a warmer atmosphere and more water vapor. The change in TOA flux is 20% less in the MG08 scheme (ΔTOA = −4.4 W m^{-2} MG08, −5.1 W m^{-2} RK98). This is partially due to less change in net cloud radiative forcing (ΔCRF = −1.2 W m^{-2} MG08, −1.6 W m^{-2} RK98). Differences in the response may be due to the lower quantity of liquid water with MG08. A full analysis of changes to the climate sensitivity from the MG08 scheme is beyond the scope of this work, but it suggests that cloud microphysics, or at least total cloud water path, may impact the response of the atmosphere to forcing.

5. Sensitivity of scheme

We further develop our analysis of the MG08 scheme by considering several sensitivity tests, including using a

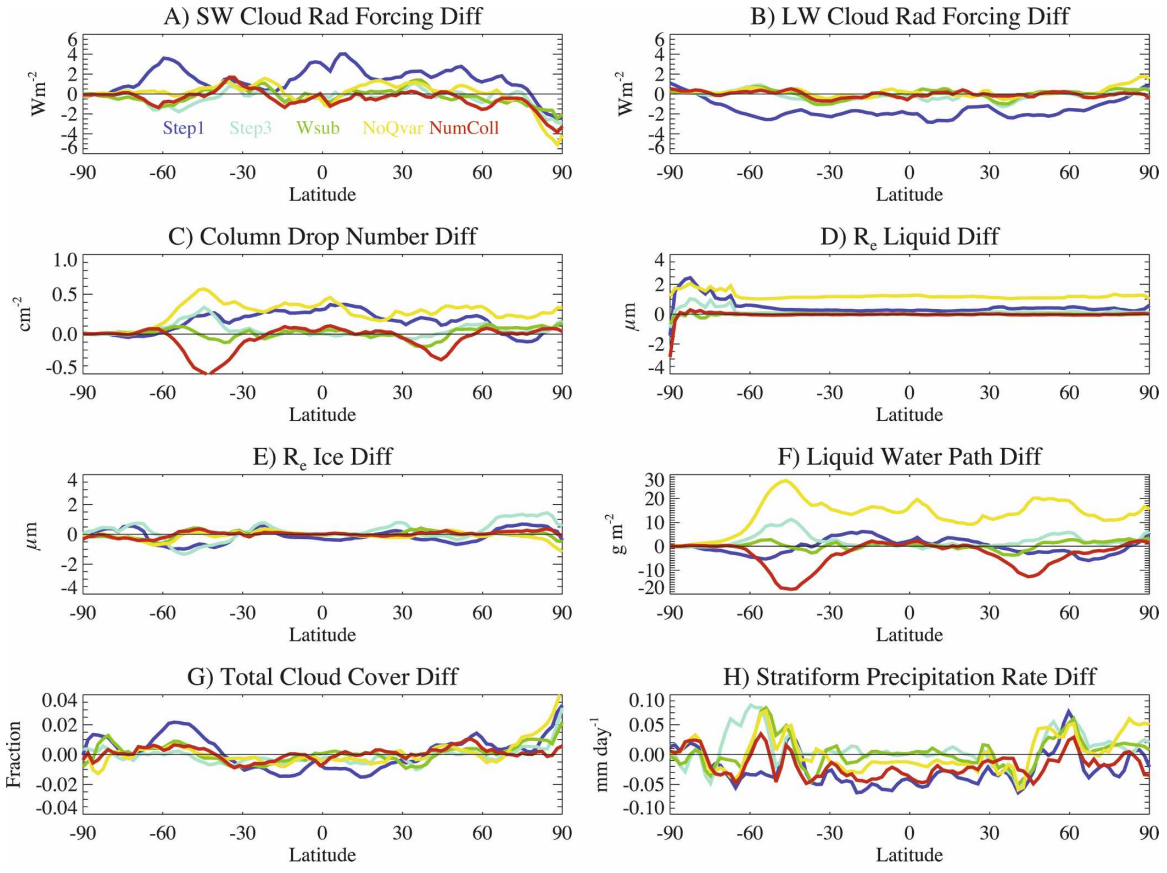

FIG. 13. Zonal-mean differences in values from the standard MG08 microphysics case. One substep (Step1: dark blue) and three steps (Step3: light blue). Higher subgrid vertical velocity (Wsub: green), no subgrid water variance (No-Qvar: yellow), and rain collection changes (NumCol: red). Variables shown are (a) shortwave cloud forcing, (b) longwave cloud forcing, (c) column cloud drop number concentration, (d) cloud-top effective radius liquid, (e) cloud-top effective radius ice, (f) total global cloud LWP, (g) total cloudiness, and (h) precipitation rate.

different number of temporal substeps in the microphysics scheme, changing the minimum value of subgrid vertical velocity, neglecting subgrid cloud water variability, changing formulation for autoconversion of rain number concentration, and changing horizontal resolution.

For numerical stability, the scheme substeps through the relatively long CAM time step (20–30 min). The standard configuration has two steps; this was found to be more numerically stable than using a single step (MG08) and was similar to using three steps. Global simulations were performed with one substep (Step1) and three substeps (Step3). Figure 13 illustrates zonal-mean differences from the standard MG08 microphysics case, and Table 3 shows global values. Figure 13 indicates that with one step there are slightly larger liquid and smaller ice particles, larger liquid number concentrations, and a lower stratiform precipitation rate (consistent with results from MG08). As noted by MG08, one step has numerical instabilities as forcing is increased. On average, this seems to produce smaller and more particles (perhaps due to increased nucleation of small particles). There are also decreases in cloud forcing. In general, the three-step case has fewer consistent differences from the standard (two-step case), which is consistent with the convergence found by MG08.

The scheme does not appear to be very sensitive to the minimum subgrid vertical velocity, specified to be 0.1 m s^{-1} in the standard configuration. A sensitivity test with the minimum set to 0.4 m s^{-1} (Wsub40) indicates very few differences from the base case (Table 3). There appear to be small shifts in stratiform precipitation toward the poles (Fig. 13h), but these are only a few percent of the peak values. One explanation for the insensitivity of the model to subgrid vertical velocity in this test is that many regions of the lower troposphere where liquid clouds are present have a zonal-mean vertical velocity greater than or equal to 0.4 m s^{-1} (Fig. 8b).

An experiment was also conducted with subgrid variability of cloud water neglected (No-Qvar case), meaning that only grid-mean values of cloud water were used to drive the microphysical process rates, rather than a distribution of cloud water as in the standard configuration (see MG08). In this case there are significant increases in the liquid water path (Fig. 13f), which globally increases 20%. There are also increases in the droplet effective radius, which compensates for the increase in the liquid water path so that the overall radiation balance is not significantly altered (Table 3).

We have investigated changes in the parameterization of rain drop number formed by droplet autoconversion. In the standard configuration, rain number increases by autoconversion only in the absence of a significant flux of precipitation from above (MG08). This was designed to mimic the rapid collection of new drizzle-size drops by existing rain or snow particles falling into the layer. In the sensitivity test (NumCol), rain number increases by autoconversion at all levels where autoconversion takes place (i.e., throughout the depth of the cloud layer), not just at cloud top. This test (NumCol) may underpredict collection. In this case, there are decreases in column cloud droplet number (Fig. 13c) and the liquid water path (Fig. 13f) in the midlatitude storm tracks, and small decreases in stratiform rain in the tropics and subtropics (Fig. 13h). These changes are also evident globally (Table 3). There are large increases in rain number (not shown) and a compensating decrease in mean rain drop size, which could have an impact on processes that depend on drop size and terminal velocity, such as scavenging of aerosols. The baseline case for rain number and size is more realistic.

We have also attempted to investigate the performance of the scheme at different horizontal resolutions. This is a difficult task, because all of the physics packages are affected by the horizontal resolution and there are subtle differences in configuration for different resolutions. Thus a simple comparison of the scheme at different resolutions will not suffice, as sensitivity of other model components will impact results along with microphysics.

To test the sensitivity to resolution, we have run model simulations at $0.9^\circ \times 1.25^\circ$, $1.9^\circ \times 2.5^\circ$, and $4^\circ \times 5^\circ$ horizontal resolution with the new and old microphysics schemes. Unfortunately, the interplay of processes in a GCM parameterization often responds differently to different resolutions. The reasons are complex but, for example, relate to different resolved processes and thus dynamical forcing at different resolutions. Our goal is to isolate sensitivity of the microphysics by comparing sensitivity using the new MG08 scheme with the overall sensitivity of the base RK98 case. We generally find that with the MG08 microphysics, the net radiation and total cloud forcing are less sensitive to resolution than in the base case. However, results also indicate that most of the sensitivity of the model is not due to the microphysics. For example, in the RK98 case, total cloudiness decreases with resolution from 61% at $4^\circ \times 5^\circ$ to 59% at $1.9^\circ \times 2.5^\circ$ to 55% at $0.9^\circ \times 1.25^\circ$. For the case with the MG08 microphysics, it is 65%, 63%, and 61%, respectively. Using either microphysics scheme, stratiform preciptiation increases by 20%–30% as resolution is increased. This is likely due to differences in resolved dynamics. Interestingly, in the base case, the total cloud liquid water path does not change with resolution, while the low-resolution ($4^\circ \times 5^\circ$) simulation has 20% less liquid water than in the higher-resolution simulations (mostly in storm track regions) using the MG08 microphysics.

The ice water path is unchanged. Particle sizes vary less than 2% with resolution. This set of tests is not definitive, but it illustrates that the new microphysics scheme is not overly sensitive to model horizontal resolution.

6. Conclusions

Results of this analysis indicate that the new parameterization described by MG08 produces reasonable single-column and global climate simulations. The scheme is stable and provides improved self-consistency of the representation of clouds. Key new features are 1) diagnostic precipitation mass, number, and hence size, which agree with available observations, and 2) that subgrid variability in water is treated in the microphysical process rates. Feature 1) is important for capturing different precipitation regimes (e.g., deep systems versus drizzle), self-consistent scavenging of aerosols and chemical species, and including precipitation species in radiation calculations. Feature 2) is important for nonlinear process rates and future coupling to cloud macrophysical schemes with explicit variability (i.e., PDF-based schemes).

The mixed-phase processes are well represented, and there are large differences in the mixed-phase transition between ice and liquid depending on region. At higher latitudes and lower altitudes, supercooled water is present down to -25°C.

Cloud droplet particle sizes are reasonable relative to available in situ and ground- based observations of stratiform clouds. Most of these observations are from stratiform clouds over oceans (marine stratocumulus) or continental stratus cloud. Additional data on other cloud types would be desirable. Attempts to derive

cloud-top variables from the model do not agree quantitatively with satellite observations, likely due to vertical gradients at cloud top and possibly due to precipitation or convective cloud particles. However, the correct morphology and variability is produced, with oceanic clouds having generally larger sizes and smaller number concentrations than points over land. The droplet effective radius is much smaller than that specified by the base model (RK98) bulk microphysics. Values of the predicted droplet effective radius using the new scheme are in general agreement with in situ observations. Cloud droplet number concentrations are also reasonable compared to observations. Concentrations are higher in regions of aerosol loading over northeast Asia, Europe, and eastern North America. Concentrations are also higher in the subtropical stratocumulus regions.

The reduction in droplet size using the scheme allows the model to achieve radiation balance with significantly less liquid water path in the atmosphere (in better agreement with available observations). It is unclear how much of an impact the lower condensed water path will have on the simulations or the response to climate change. Cloud forcing appears to respond to surface changes differently using the new microphysics, which may impact simulated climate sensitivity. A quantitative analysis of this change is a subject of ongoing work.

In the model, cirrus clouds at high altitude have effective radii of 20–40 μm. There is a long tail to the distribution and a significant number of points that reach 100 μm. In this paper, we did not compare the modeled and observed cloud ice sizes and number concentrations, given the difficulty of observing small ice particles and the wide range of uncertainty (over several orders of magnitude) in estimates of the concentration of small ice particles (Heymsfield 2007). Reducing uncertainty in the observations of small ice particles in the future will help to constrain the modeled values. Mean snow particle sizes (from 100 to 1000 μm) are consistent with in situ observations. The model is able to produce distinct differences in rain drop size consistent with observations for different regimes, namely, small drops in drizzling low-level clouds and large drops formed by melted snow in deeper cloud systems. The temporal- and zonal-mean values of rain drop size over the globe are between values observed for these two regimes.

Sensitivity tests indicate that the ability of the model to capture observed rain size distributions for these two regimes is because of its inclusion of rain number concentration, which is neglected in most models. Inclusion of rain number concentration has less impact on cloud properties and radiative forcing, but its impact on the ability to predict rain size distribution may have important consequences for aerosol interactions, including wet scavenging. Inclusion of snow number concentration appears to have less impact than it does for rain, but it may be more important in conditions with low ice nucleus concentrations, which were not considered here.

Overall, sensitivity tests indicate the scheme is stable. It performs slightly better when at least two substeps are utilized over the time step. The scheme appears to be most sensitive to the description of subgrid variance in the microphysical process rates. This highlights the importance of nonlinear processes in the microphysics. Similar sensitivity results are found for individual IOP locations as well as for the global simulations. The scheme does not appear to be overly sensitive to horizontal resolution, and it responds in a way that was similar to the response of the RK98 microphysics scheme, with the exception of a reduced liquid water path in the lowest resolution examined ($4^\circ \times 5^\circ$). The new MG08 scheme is less sensitive to resolution than other model components (either the physics or dynamics).

All of these simulations were performed with fixed aerosol distributions. Future work on the scheme will document the sensitivity of the MG08 microphysics and the overall simulation to changes in the aerosols and describe aerosol–cloud interactions. We also intend to couple the crystal nucleation to the aerosol distribution following Liu et al. (2007) to improve the treatment of ice clouds (cirrus and anvil) in the new scheme and correct inconsistencies with the radiation code. Preliminary analysis indicates that the scheme has the right sensitivity to aerosols: as the aerosols increase, cloud particle sizes decrease and particle number concentrations increase.

Acknowledgments. Thanks to Q. Han for supplying AVHRR data and G. Mace for providing the retrieval data from the ARM SGP site. Thanks to S. Vavrus for use of his parameterization and discussions. Thanks to N. Loeb for pointing us to CERES–MODIS data, and to R. Wood for use of MODIS retrievals. Thanks to P. J. Rasch and R. Neale for comments. Special thanks to Jay Fein, NSF for supporting this effort. This work was also supported by NSF Grant 0603539. H. Morrison would also like to acknowledge support from the NCAR Advanced Study Program and NASA MAP Grant NNG06GBB1G. S. J. Ghan was supported by the U.S. Department of Energy Atmospheric Radiation Measurement Program, which is part of the DOE Climate Change Research Program. The Pacific Northwest National Laboratory is operated for the DOE by

Battelle Memorial Institute under Contract DE-AC06-76RLO 1830.

REFERENCES

Abdul-Razzak, H., and S. J. Ghan, 2000: A parameterization of aerosol activation 2. Multiple aerosol types. *J. Geophys. Res.,* **105,** 6837–6844.

——, ——, and C. Rivera-Carpio, 1998: A parameterization of aerosol activation 1. Single aerosol type. *J. Geophys. Res.,* **103,** 6123–6131.

Bony, S., and Coauthors, 2006: How well do we understand and evaluate climate change feedback processes? *J. Climate,* **19,** 3445–3482.

Boville, B. A., P. J. Rasch, J. J. Hack, and J. R. McCaa, 2006: Representation of clouds and precipitation processes in the Community Atmosphere Model version 3 (CAM3). *J. Climate,* **19,** 2184–2198.

Bower, K. N., and T. W. Choularton, 1992: A parameterization of the effective radius of ice-free clouds for use in global climate models. *Atmos. Res.,* **27,** 305–339.

Brenguier, J.-L., H. Pawlowska, and L. Schüller, 2003: Cloud microphysical and radiative properties for parameterization and satellite monitoring of the indirect effect of aerosol on climate. *J. Geophys. Res.,* **108,** 8632, doi:10.1029/2002JD002682.

Cess, R. D., and Coauthors, 1990: Intercomparison and interpretation of climate feedback processes in 19 atmospheric general circulation models. *J. Geophys. Res.,* **95,** 16 601–16 615.

Charlson, R. J., J. E. Lovelock, M. O. Andreae, and S. G. Warren, 1987: Oceanic phytoplankton, atmospheric sulphur, cloud albedo and climate. *Nature,* **326,** 655–661.

Collins, W. D., P. J. Rasch, B. E. Eaton, B. Khattatov, J.-F. Lamarque, and C. S. Zender, 2001: Simulating aerosols using a chemical transport model with assimilation of satellite retrievals: Methodology for INDOEX. *J. Geophys. Res.,* **106,** 7313–7336.

——, ——, ——, D. W. Fillmore, J. T. Kiehl, T. C. Beck, and C. S. Zender, 2002: Simulation of aerosol distributions and radiative forcing for INDOEX: Regional climate impacts. *J. Geophys. Res.,* **107,** 8028, doi:10.1029/2000JD000032.

——, and Coauthors, 2004: Description of the NCAR community atmosphere model (CAM3.0). Tech. Rep. NCAR/TN-464+STR, National Center for Atmospheric Research, 226 pp. [Available online at http://www.ccsm.ucar.edu/models/atm-cam.]

——, and Coauthors, 2006: The formulation and atmospheric simulation of the Community Atmosphere Model: CAM3. *J. Climate,* **19,** 2122–2161.

Cooper, W. A., 1986: Ice initiation in natural clouds. *Precipitation Enhancement—A Scientific Challenge, Meteor. Monogr.,* No. 21, Amer. Meteor. Soc., 29–32.

Ebert, E. E., and J. A. Curry, 1992: A parameterization of cloud optical properties for climate models. *J. Geophys. Res.,* **97,** 3831–3836.

Field, P. R., R. J. Hogan, R. A. Brown, A. J. Illingworth, T. W. Choularton, and R. J. Cotton, 2005: Parameterization of ice-particle size distributions for mid-latitude stratiform cloud. *Quart. J. Roy. Meteor. Soc.,* **131,** 1997–2017.

Ghan, S. J., and Coauthors, 2000: A comparison of single column simulations of summertime midlatitude continental convection. *J. Geophys. Res.,* **105,** 2091–2124.

——, R. C. Easter, J. Hudson, and F.-M. Breon, 2001: Evaluation of aerosol indirect radiative forcing in MIRAGE. *J. Geophys. Res.,* **106,** 5317–5334.

Gultepe, I., and G. A. Isaac, 2004: Aircraft observations of cloud droplet number concentration: Implications for climate studies. *Quart. J. Roy. Meteor. Soc.,* **130,** 2377–2390.

Han, Q., W. B. Rossow, J. Chou, and R. W. Welch, 1998: Global variation of column droplet concentration in low-level clouds. *Geophys. Res. Lett.,* **25,** 1419–1422.

Heymsfield, A. J., 2003: Properties of tropical and midlatitude ice cloud particle ensembles. Part II: Applications for mesoscale and climate models. *J. Atmos. Sci.,* **60,** 2592–2611.

——, 2007: On measurements of small ice particles in clouds. *Geophys. Res. Lett.,* **34,** L23812, doi:10.1029/2007GL030951.

——, and A. Banssemer, 2007: Refinements to ice particle mass dimensional and terminal velocity relationships for ice clouds: Part I: Temperature dependence. *J. Atmos. Sci.,* **64,** 1047–1067.

Houze, R. A., P. V. Hobbs, P. H. Herzegh, and D. B. Parsons, 1979: Size distributions of precipitation particles in frontal clouds. *J. Atmos. Sci.,* **36,** 156–162.

Kim, B.-G., S. E. Schwartz, M. A. Miller, and Q. Min, 2003: Effective radius of cloud droplets by ground-based remote sensing: Relationship to aerosol. *J. Geophys. Res.,* **108,** 4740, doi:10.1029/2003JD003721.

Lesht, B. M., and J. C. Liljegren, 1997: Comparison of precipitable water vapor measurements obtained by microwave radiometry and radiosondes at the Southern Great Plains Cloud and Radiation Testbed Site. *Proc. Sixth Atmospheric Radiation Measurement (ARM) Science Team Meeting,* San Antonio, TX, Department of Energy, CONF-9603149 UC-402, 165–168.

Lin, S.-J., and R. B. Rood, 1996: Multidimensional flux-form semi-Lagrangian transport schemes. *Mon. Wea. Rev.,* **124,** 2046–2070.

Liu, X., J. E. Penner, S. J. Ghan, and M. Wang, 2007: Inclusion of ice microphysics in the NCAR Community Atmospheric Model version 3 (CAM3). *J. Climate,* **20,** 4526–4547.

Lohmann, U., J. Feichter, J. Penner, and R. Leaitch, 2000: Indirect effect of sulfate and carbonaceous aerosols: A mechanistic treatment. *J. Geophys. Res.,* **105,** 12 193–12 206.

——, P. Stier, C. Hoose, S. Ferrachat, E. Roeckner, and J. Zhang, 2007: Cloud microphysics and aerosol indirect effects in the global climate model ECHAM5-HAM. *Atmos. Chem. Phys.,* **7,** 3719–3761.

Mace, G. G., and Coauthors, 2006: Cloud radiative forcing at the Atmospheric Radiation Measurement Program Climate Research Facility: 1. Technique, validation, and comparison to satellite-derived diagnostic quantities. *J. Geophys. Res.,* **111,** D11S90, doi:10.1029/2005JD005921.

Mahowald, N. M., J.-F. Lamarque, X. X. Tie, and E. Wolff, 2006: Sea-salt aerosol response to climate change: Last Glacial Maximum, preindustrial, and doubled carbon dioxide climates. *J. Geophys. Res.,* **111,** D05303, doi:10.1029/2005JD006459.

Marshall, J. S., and W. M. Palmer, 1948: The distribution of raindrops with size. *J. Meteor.,* **5,** 165–166.

Martin, G. M., D. W. Johnson, and A. Spice, 1994: The measurement and parameterization of effective radius of droplets in warm stratocumulus clouds. *J. Atmos. Sci.,* **51,** 1823–1842.

McFarquhar, G. M., G. Zhang, M. R. Poellot, G. L. Kok, R. McCoy, T. P. Tooman, A. M. Fridlind, and A. J. Heymsfield, 2007: Ice properties of single-layer stratocumulus during the Mixed-Phase Arctic Cloud Experiment: 1. Observations. *J. Geophys. Res.,* **112,** D24201, doi:10.1029/2007JD008633.

Morrison, H., and J. O. Pinto, 2006: Intercomparison of bulk cloud microphysics schemes in mesoscale simulations of springtime Arctic mixed-phase stratiform clouds. *Mon. Wea. Rev.,* **134,** 1880–1900.

——, and A. Gettelman, 2008: A new two-moment bulk stratiform cloud microphysics scheme in the Community Atmosphere Model, version 3 (CAM3). Part I: Description and numerical tests. *J. Climate,* **21,** 3642–3659.

Pawlowska, H., W. W. Grabowski, and J.-L. Brenguier, 2006: Observations of the width of cloud droplet spectra in stratocumulus. *Geophys. Res. Lett.,* **33,** L19810, doi:10.1029/2006GL026841.

Prenni, A. J., and Coauthors, 2007: Can ice-nucleating aerosols affect Arctic seasonal climate? *Bull. Amer. Meteor. Soc.,* **88,** 541–550.

Rasch, P. J., and J. E. Kristjánsson, 1998: A comparison of CCM3 model climate using diagnosed and predicted condensate parameterizations. *J. Climate,* **11,** 1587–1614.

——, and Coauthors, 2006: A characterization of tropical transient activity in the CAM3 atmospheric hydrologic cycle. *J. Climate,* **19,** 2222–2242.

Ringer, M. A., and Coauthors, 2006: Global mean cloud feedbacks in idealized climate change experiments. *Geophys. Res. Lett.,* **33,** L07718, doi:10.1029/2005GL025370.

Rotstayn, L. D., 1997: A physically based scheme for the treatment of stratiform clouds and precipitation in large-scale models. I: Description and evaluation of the microphysical processes. *Quart. J. Roy. Meteor. Soc.,* **123,** 1227–1282.

Sengupta, M., E. E. Clothiaux, T. P. Ackerman, S. Kato, and Q. Min, 2003: Importance of accurate liquid water path for estimation of solar radiation in warm boundary layer clouds: An observational study. *J. Climate,* **16,** 2997–3009.

Slingo, A. A., 1989: A GCM parameterization for the shortwave radiative properties of clouds. *J. Atmos. Sci.,* **46,** 1419–1427.

Slingo, J. M., 1987: The development and verification of a cloud prediction scheme for the ECMWF model. *Quart. J. Roy. Meteor. Soc.,* **113,** 899–927.

Stephens, G. L., 2005: Cloud feedbacks in the climate system: A critical review. *J. Climate,* **18,** 237–273.

Twomey, S., 1977: The influence of pollution on the shortwave albedo of clouds. *J. Atmos. Sci.,* **34,** 1149–1152.

Vavrus, S., and D. Waliser, 2008: An improved parameterization for simulating Arctic cloud amount in the CCSM3 climate model. *J. Climate,* in press.

Wood, R., 2000: Parameterization of the effect of drizzle upon the droplet effective radius in stratocumulus clouds. *Quart. J. Roy. Meteor. Soc.,* **126,** 3309–3324.

——, 2005: Drizzle in stratiform boundary layer clouds. Part I: Vertical and horizontal structure. *J. Atmos. Sci.,* **62,** 3011–3033.

——, K. K. Comstock, C. S. Bretherton, C. Cornish, J. Tomlinson, D. R. Collins, and C. Fairall, 2008: Open cellular structure in marine stratocumulus sheets. *J. Geophys. Res.*, in press. doi:10.1029/2007JD009371.

Xie, S., and Coauthors, 2005: Simulations of midlatitude frontal clouds by single-column and cloud-resolving models during the Atmospheric Radiation Measurement March 2000 cloud intensive operation period. *J. Geophys. Res.,* **110,** D15S03, doi:10.1029/2004JD005119.

Zender, C. S., H. Bian, and D. Newman, 2003: Mineral Dust Entrainment and Deposition (DEAD) model: Description and 1990s dust climatology. *J. Geophys. Res.,* **108,** 4416, doi:10.1029/2002JD002775.

Zhang, M., W. Lin, C. S. Bretherton, J. J. Hack, and P. J. Rasch, 2003: A modified formulation of fractional stratiform condensation rate in the NCAR Community Atmospheric Model (CAM2). *J. Geophys. Res.,* **108,** 4035, doi:10.1029/2002JD002523.

Zuidema, P., and Coauthors, 2005: An Arctic springtime mixed-phase cloudy boundary layer observed during SHEBA. *J. Atmos. Sci.,* **62,** 160–176.